

BINARY BLACK HOLE ACCRETION FROM A CIRCUMBINARY DISK: GAS DYNAMICS INSIDE THE CENTRAL CAVITY

BRIAN D. FARRIS^{1,2}, PAUL DUFFELL¹, ANDREW I. MACFADYEN¹, AND ZOLTAN HAIMAN²

¹ Center for Cosmology and Particle Physics, New York University, New York, NY, USA

² Department of Astrophysics, Columbia University, New York, NY, USA

Received 2013 October 1; accepted 2014 January 28; published 2014 February 24

ABSTRACT

We present the results of two-dimensional (2D) hydrodynamical simulations of circumbinary disk accretion using the finite-volume code *DISCO*. This code solves the 2D viscous Navier–Stokes equations on a high-resolution moving mesh which shears with the fluid flow, greatly reducing advection errors in comparison with a fixed grid. We perform a series of simulations for binary mass ratios in the range $0.026 \leq q \leq 1.0$, each lasting longer than a viscous time so that we reach a quasi-steady accretion state. In each case, we find that gas is efficiently stripped from the inner edge of the circumbinary disk and enters the cavity along accretion streams, which feed persistent “mini disks” surrounding each black hole. We find that for $q \gtrsim 0.1$, the binary excites eccentricity in the inner region of the circumbinary disk, creating an overdense lump which gives rise to enhanced periodicity in the accretion rate. The dependence of the periodicity on mass ratio may provide a method for observationally inferring mass ratios from measurements of the accretion rate. We also find that for all mass ratios studied, the magnitude of the accretion onto the secondary is sufficient to drive the binary toward larger mass ratio. This suggests a mechanism for biasing mass-ratio distributions toward equal mass.

Key words: accretion, accretion disks – black hole physics

Online-only material: color figures

1. INTRODUCTION

It is currently believed that supermassive black holes (SMBHs) with masses between 10^6 and $10^9 M_\odot$ reside in nearly all nearby galaxy nuclei (Kormendy & Richstone 1995; Ferrarese & Ford 2005). Furthermore, galaxy mergers are believed to give rise to bound SMBH binary systems in the merged galaxy remnant, following a phase of dynamical friction in which the SMBHs become gravitationally bound (Begelman et al. 1980; Roos 1981; Merritt & Milosavljević 2005). Such galaxy mergers occur commonly in models of hierarchical structure formation (Haehnelt & Kauffmann 2002).

It is expected that there is an abundance of dense gas in the nuclei of merged galaxies (Barnes & Hernquist 1992; Springel et al. 2005) and that this gas can form a circumbinary accretion disk (Artymowicz & Lubow 1996; Armitage & Natarajan 2002; Milosavljević & Phinney 2005). In this scenario, tidal torques from the binary tend to drive gas outward, clearing an empty hollow around the binary. Viscous torques transport angular momentum outward in the disk, allowing gas to flow inward and refill the cavity. The balance of tidal and viscous torques determines the location of the inner edge of the circumbinary disk at $r \approx 2a$, where a is the binary separation. This balance can be maintained, provided the timescale t_{gw} for inspiral of the binary due to gravitational wave (GW) emission is much longer than the viscous timescale of the disk, t_{visc} . This is known as the “pre-decoupling” epoch, and is the focus of this paper. Such binaries may provide a unique opportunity to observe various time-dependent and kinematic electromagnetic signatures originating from the interaction of the binary with the surrounding accretion disk. The gravitational radiation originating from the SMBH binary inspiral should also be detectable by Pulsar Timing Arrays (Hobbs et al. 2010). For massive ($\sim 10^8$ – $10^9 M_\odot$) binaries at redshift $z \approx 1$, these sources are typically expected around the time of decoupling (Kocsis &

Sesana 2011; Tanaka et al. 2012; Lommen 2012; Sesana et al. 2012). Typical binary black hole (BH) GW sources detected by a space interferometer at higher frequencies, such as eLISA (Amaro-Seoane et al. 2013), would be well past the decoupling epoch, but the lowest-mass, unequal-mass eLISA sources may still be surrounded by a circumbinary disk (Barausse & Rezzolla 2008; Yunes et al. 2011; Kocsis et al. 2012a).

Aspects of this problem have been studied analytically (Goldreich & Tremaine 1980; Artymowicz & Lubow 1994; Ivanov et al. 1999; Armitage & Natarajan 2002; Milosavljević & Phinney 2005; Chang et al. 2010; Haiman et al. 2009; Shapiro 2010, 2013; Liu & Shapiro 2010; Kocsis et al. 2012a, 2012b; Tanaka 2013), often using approximate angle-averaged tidal torque formulae. While this technique has proven very useful in highlighting qualitative features of the accretion, two-dimensional (2D) or three-dimensional (3D) simulations are required to capture the effect of gas streams which may be stripped off the inner cavity, accreting directly onto the binary. Prior numerical simulations have been performed in 2D (MacFadyen & Milosavljević 2008, hereafter MM08), (D’Orazio et al. 2013) and in 3D (Hayasaki et al. 2007; Cuadra et al. 2009; Farris et al. 2011, 2012; Noble et al. 2012; Shi et al. 2012; Roedig et al. 2012; Bode et al. 2012; Giacomazzo et al. 2012). However, many simulations to date have excised the innermost region surrounding the binary and imposed an inner boundary condition, potentially neglecting important dynamics occurring inside the excised region. Such simulations are also unable to track the accretion onto each individual BH. All examples of simulations which capture the inner cavity have either been performed with smoothed particle hydrodynamics (SPH) codes (Hayasaki et al. 2007; Cuadra et al. 2009; Nixon et al. 2011; Roedig et al. 2012), or have been restricted to relatively small numbers of orbits (Giacomazzo et al. 2012; Farris et al. 2012). This will be the first 2D study including the inner cavity, using shock-capturing Godunov-type methods

evolving thin ($h/r \sim 0.1$) disks over the viscous timescales necessary to accurately capture the steady-state accretion at high resolution. Such methods have already been shown to be effective for the related problem of gap opening in protoplanetary disks (Duffell & MacFadyen 2013).

Our simulations of viscous disk accretion onto a binary use *DISCO*, a high-resolution, moving-mesh finite-volume code (Duffell & MacFadyen 2011, 2012, 2013) in which we impose no inner boundary condition, so that the BHs are included in the computational domain. Because grid cells move azimuthally with the fluid, we minimize advection errors, allowing us to accurately capture dynamics of accretion streams which penetrate into the cavity. We measure accretion rates onto each BH and compare results for mass ratios $q \equiv m_2/m_1$ between 0.026 and 1.0.

The structure of the paper is as follows. In Section 2, we review the viscous-hydrodynamic evolution equations and summarize our numerical methods. In Section 3 we describe our results and compare them with previous work. In Section 4 we summarize our conclusions and outline topics for future work. Throughout the paper, we adopt units in which $G = c = 1$.

2. METHODS

All simulations are performed using the *DISCO* code (Duffell & MacFadyen 2012, 2013). In regions where the Keplerian motion dominates, the method is effectively Lagrangian, and advection errors are greatly reduced. *DISCO* is based on the *TESS* code (Duffell & MacFadyen 2011), and shares many of its features. For more details on the methods employed by *DISCO* and *TESS*, see Duffell & MacFadyen (2011, 2012).

2.1. Basic Equations

We model the flow of a thin accretion disk onto a SMBH binary using the vertically averaged, 2D Navier–Stokes equations,

$$\partial_t \Sigma + \frac{1}{r} \partial_r (r \Sigma v_r) + \frac{1}{r} \partial_\phi (\Sigma v_\phi) = 0 \quad (1)$$

$$\begin{aligned} \partial_t (\Sigma v_r) + \frac{1}{r} \partial_r (r (\Sigma v_r^2 + P)) + \frac{1}{r} \partial_\phi (\Sigma v_r v_\phi) \\ = (\Sigma v_\phi^2 + P)/r + F_r^{\text{vis}} + F_r^{\text{grav}} \end{aligned} \quad (2)$$

$$\begin{aligned} \partial_t (r \Sigma v_\phi) + \frac{1}{r} \partial_r (r^2 (\Sigma v_r v_\phi)) + \frac{1}{r} \partial_\phi (r (\Sigma v_\phi^2 + P)) \\ = r (F_\phi^{\text{vis}} + F_\phi^{\text{grav}}). \end{aligned} \quad (3)$$

Here Σ is the surface density, P is the vertically integrated pressure, and v_r and v_ϕ are the radial and azimuthal fluid velocities, respectively. F_ϕ^{vis} and F_ϕ^{grav} are the viscous and gravitational source terms, which are described in Sections 2.2 and 2.3. The pressure is set to enforce a locally isothermal equation of state of the form,

$$\begin{aligned} c_s &= \left(\frac{P}{\Sigma} \right)^{1/2} = (h/r) \left(\frac{M_1}{r_1} + \frac{M_2}{r_2} \right)^{1/2} \\ &\approx \begin{cases} (h/r)(r_1 \Omega_{k,1}) & r_1 \ll r_2 \\ (h/r)(r_2 \Omega_{k,2}) & r_2 \ll r_1 \\ (h/r)(r \Omega_k) & r \gg a. \end{cases} \end{aligned} \quad (4)$$

Here r_1 and r_2 are the distances from the BHs labeled bh_1 and bh_2 respectively, $\Omega_{k,1}$ and $\Omega_{k,2}$ are the corresponding Keplerian

angular velocities, r is the distance from the origin, and Ω_k is the Keplerian orbital velocity around a central point mass of mass $M = m_1 + m_2$, and a is the binary separation. Following MacFadyen & Milosavljević (2008) and D’Orazio et al. (2013), we choose $h/r = \text{const} = 0.1$. This choice of temperature profile matches that of a constant $h/r = 0.1$ α -disk near each individual BH in the limit $r_{1,2} \ll r$, and that of a constant $h/r = 0.1$ circumbinary α -disk in the limit that $r \gg r_{1,2}$. We note that α -disks may be colder and have $h/r \sim 10^{-3}$. However, simulating disks numerically with $h/r = 10^{-3}$ is currently prohibitively challenging, and our choice of $h/r = 0.1$ allows for comparison with previous work (Artymowicz & Lubow 1994; MacFadyen & Milosavljević 2008; D’Orazio et al. 2013). In future work, we intend to investigate changes which emerge at smaller h/r , as well as relaxing the assumption that h/r is constant everywhere, as the gas in each circumstellar mini disk may in fact be hotter than the circumbinary gas.

In each of our simulations, we assume that the disk mass is small compared to the binary mass, $M_{\text{disk}} \ll M$ so that we may neglect the self gravity of the gas as well as changes in the binary orbit due to torques from the gas. If we consider our smallest mass ratio $q = 0.026$ and consider the extreme case of a binary of mass $M = 10^9 M_\odot$ and separation $a = 10^3 GM/c^2$ accreting at the Eddington rate with an efficiency of $\eta = 0.1$, with the secondary dominating the accretion, we find the fractional growth of the secondary over the course of a simulation lasting 500 orbits,

$$\begin{aligned} \frac{\Delta M_2}{M_2} &= 0.01 \left(\frac{q}{0.026} \right)^{-1} \left(\frac{M}{10^9 M_\odot} \right) \\ &\times \left(\frac{a}{10^3 GM/c^2} \right)^{3/2} \left(\frac{\eta}{0.1} \right)^{-1}. \end{aligned} \quad (5)$$

For larger mass ratios, smaller binary masses, lower accretion rates, and separations closer to decoupling at $a \sim 100 GM/c^2$, $\Delta M_2/M_2$ decreases. We conclude that it is reasonable to neglect the influence of the gas on the binary orbit for a large range of physically realistic parameters. Throughout each simulation, we also assume that the binary orbit is circular with constant separation a . This assumption may be relaxed in future work.

2.2. Viscosity Prescription

We choose an α -law viscosity of the form (Shakura & Sunyaev 1973),

$$\nu = \alpha c_s^2 \Omega_k^{-1}, \quad (6)$$

where $\alpha = 0.1$ is chosen for this study. Close to the binary, we expect that as the flow develops a strong radial component in the streams, the α -viscosity prescription becomes inapplicable. In fact, there is some evidence from 3D MHD simulations of accretion onto binaries that the effective α may increase significantly near the inner edge of the disk and inside the cavity (Shi et al. 2012; Noble et al. 2012). An analogous effect is also associated with the position of the innermost stable circular orbit in fully relativistic calculations (Krolik 1999; Gammie 1999; Noble et al. 2010; Penna et al. 2013). However, the solution should not be sensitive to the details of the viscosity prescription inside the cavity, as the flow in this region is dominated by variations occurring on the orbital timescale, which is much shorter than the viscous timescale. Thus, viscosity is not expected to play an important role until the gas settles into the “mini disks” around each individual BH.

We therefore treat the role of viscosity in driving accretion of the mini disks with an accretion prescription (see Section 2.4).

The presence of viscosity modifies the hydrodynamic equations by adding a viscous component to the stress tensor given by

$$\sigma_{ij} = \Sigma v (\nabla_i v_j + \nabla_j v_i - \delta_{ij} \nabla \cdot v), \quad (7)$$

where we have set the bulk viscosity to 0. Expressing components of the divergence of the viscous stress tensor in cylindrical coordinates, we find (see Appendix A of D’Orazio et al. 2013),

$$F_r^{\text{vis}} \equiv (\nabla \cdot \sigma)_r = \frac{1}{r^2} \partial_r \left(r \Sigma v \left(r \partial_r v_r - v_r + \Omega r \frac{\partial_\phi P}{P} \right) \right) + \frac{1}{r^2} \partial_\phi \left(\Sigma v \left(\partial_\phi v_r - \Omega r^2 \left(\frac{7}{2} \frac{1}{r} + \frac{\partial_r P}{P} \right) \right) \right) \quad (8)$$

$$F_\phi^{\text{vis}} \equiv (\nabla \cdot \sigma)_\phi = \frac{1}{r} \partial_r \left(r \Sigma v \left(r^2 \partial_r \Omega - v_r \frac{\partial_\phi P}{P} \right) \right) + \frac{1}{r} \partial_\phi \left(\Sigma v \left(r \partial_\phi \Omega + r v_r \left(\frac{7}{2} \frac{1}{r} + \frac{\partial_r P}{P} \right) \right) \right), \quad (9)$$

where we use gradients of fluid velocity and pressure which have been computed for the reconstruction step (Duffell & MacFadyen 2011). We have used the following relations, which can be derived from Equation (6),

$$\frac{\partial_r (r^2 \Sigma v)}{r^2 \Sigma v} = \frac{7}{2} \frac{1}{r} + \frac{\partial_r P}{P} \quad (10)$$

$$\frac{\partial_\phi (r^2 \Sigma v)}{r^2 \Sigma v} = \frac{\partial_\phi P}{P}. \quad (11)$$

2.3. Gravity

The gravitational source terms are given by:

$$F_r^{\text{grav}} = -\Sigma \frac{\partial \Phi}{\partial r} \quad (12)$$

$$F_\phi^{\text{grav}} = -\frac{\Sigma}{r} \frac{\partial \Phi}{\partial \phi} \quad (13)$$

where the Φ is the Newtonian gravitational potential due to the binary,

$$\Phi(r, \phi) = -\frac{M_1}{(|\mathbf{r} - \mathbf{r}_{bh1}|^2 + \epsilon_s^2)^{1/2}} - \frac{M_2}{(|\mathbf{r} - \mathbf{r}_{bh2}|^2 + \epsilon_s^2)^{1/2}}. \quad (14)$$

Here, we have followed Duffell & MacFadyen (2013), Tanaka et al. (2002), Masset (2002), and Müller et al. (2012) and used a “vertically averaged” potential which attempts to account for corrections to the gravitational force near each point mass due to the nonzero thickness of the disk. This choice of potential also conveniently avoids divergences at the location of each point mass. In each of our simulations, we choose a smoothing length $\epsilon_s/a = 0.05$.

2.4. Accretion Prescription

Inside the cavity, matter accumulates near each BH and forms “mini disks” of gas orbiting the individual BHs. In order to achieve a quasi-steady state, we must account for the draining of these “mini disks” due to accretion onto each BH. In the absence of a fully relativistic code in which the flow across the event horizon can be resolved, this necessitates an accretion prescription. Our simulation grid is composed of concentric annuli centered about the *origin*, making it impractical to define a precise boundary around each BH within which to completely remove fluid. Instead, fluid is removed smoothly from the vicinity of each BH by treating each mini disk as an alpha-disk with $h/r = 0.1$ and $\alpha = 0.1$, and compute the viscous timescale at cells near each BH. The viscous timescale for bh_i is,

$$t_{\text{vis},i} = \frac{2}{3} \frac{r_i^2}{v_i} = \frac{1}{3\pi} \frac{1}{\alpha (h/r)^2} \left(\frac{r_i}{a} \right)^{3/2} \mu_i^{-1/2} t_{\text{bin}}, \quad (15)$$

where r_i is the distance from bh_i , $\mu_i \equiv m_i/M$ is the ratio of the mass of bh_i to the total binary mass, and t_{bin} is the binary orbital period. When $r_i/a < 0.5$ we add a source term to the right hand side of the continuity equation of the form,

$$\left(\frac{d\Sigma}{dt} \right)_{\text{sink},i} = -\frac{\Sigma}{t_{\text{vis},i}}. \quad (16)$$

This removes fluid from the vicinity of each BH at the rate expected according to the α -disk model. The removed fluid is eliminated from the simulation, and the amount removed is monitored as a measure of the accretion rate. We have experimented with varying the radius within which we apply the accretion prescription and find that the results are not sensitive to this parameter. This is expected, as $d\Sigma/dt \propto \Sigma r_i^{-3/2}$, and Σ itself is peaked near each BH. Thus, the majority of the fluid which is removed comes from very close the BHs.

2.5. Initial Setup

Following MM08, we use an initial density profile of the form

$$\Sigma(r, t_0) = \Sigma_0 \left(\frac{r}{r_s} \right)^{-3} \exp \left[-\left(\frac{r}{r_s} \right)^{-2} \right] \quad (17)$$

and a near-Keplerian velocity profile, modified to account for binary torques and pressure gradients,

$$\Omega^2 \approx \Omega_k^2 \left(1 + \frac{3}{16} (r/a)^{-2} \right)^2 + \frac{1}{r\Sigma} \frac{dP}{dr}. \quad (18)$$

We also add radial velocity to account for viscous drift,

$$v_r = \frac{2}{r^2 \Omega \Sigma} \frac{\partial (r^2 \sigma_{r\phi})}{\partial r}. \quad (19)$$

Note that our initial setup exactly mirrors that of MM08, except that we choose $\alpha = 0.1$, instead of $\alpha = 0.01$. The main effect of this choice is to shorten the viscous timescale by a factor of 10. However, as the viscous timescale is still many times the orbital period, qualitative features of the flow are expected to remain insensitive to the choice of α .

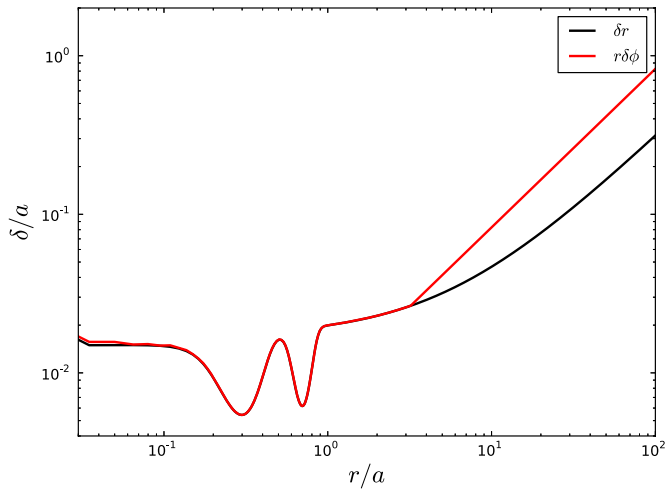


Figure 1. Grid cell sizes δr (black), and $r\delta\phi$ (red) vs. radius for the $q = 0.43$ case. Grid spacing increases roughly logarithmically with radius, and resolution is further increased in annuli near each BH, located at the two sharp minima near $r/a = 0.3$ and $r/a = 0.7$.

(A color version of this figure is available in the online journal.)

For each of our simulations, we exploit the flexibility of the *DISCO* code in choosing the grid structure. Outside the cavity, the radial grid spacing increases approximately logarithmically, allowing us to concentrate computational resources on the flow in the inner regions of the disk. Inside the cavity, we also increase the resolution in the annuli surrounding each BH, in order to maximize accuracy near each point mass. At all radii, we chose our azimuthal grid spacing such that the aspect ratio of each cell is kept approximately 1, unless this requires a number of azimuthal grid cells $N_\phi > 760$, in which case we cap the number of ϕ -zones and set $N_\phi = 760$. We have chosen to cap N_ϕ at 760 zones because this ensures that the aspect ratio is close to unity everywhere inside the cavity, where strongly non-axisymmetric structures form, while allowing for fewer zones outside the cavity. In Figure 1, we plot the cell spacing in the r and ϕ direction versus radius for the $q = 0.43$ case in order to illustrate the grid setup.

3. RESULTS

3.1. Shear Viscosity Test

In order to test our viscosity implementation, we have performed a “Cartesian shear test” similar to the one described in Section A7 of D’Orazio et al. (2013) in which we follow the viscous spreading of a shearing velocity profile. As initial data we choose constant density and pressure

$$\rho = 1.0 \quad (20)$$

$$P = 0.1 \quad (21)$$

and a velocity profile of the form

$$v^x = 0 \quad (22)$$

$$v^y = \exp\left(-\frac{(x - x_0)^2}{\sigma^2}\right), \quad (23)$$

where $\sigma = 0.5$. The most notable difference between our test and that of D’Orazio et al. (2013) is that we choose a viscosity

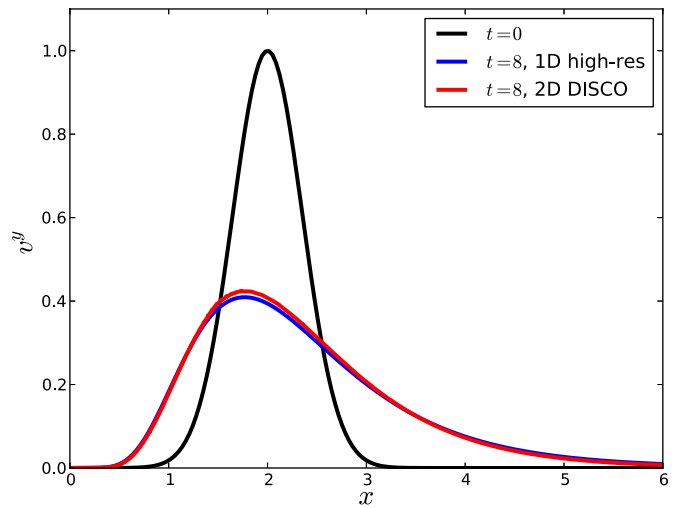


Figure 2. Results of Cartesian shear test. The black curve denotes the initial velocity profile at $t = 0$, the blue curve denotes the semi-analytic solution obtained from a high-resolution 1D solver at $t = 8.0$, and the red curve denotes the results of the *DISCO* code $t = 8.0$.

(A color version of this figure is available in the online journal.)

profile of the form,

$$v = v_0 \frac{\Gamma P}{\rho} x^2. \quad (24)$$

This choice was made in order to test the ability of *DISCO* to accurately treat a spatially varying viscosity, as is present in an α -disk. We perform this test using the cylindrical grid employed by *DISCO*, thus testing the balance of all components of the viscous forces and hydrodynamic fluxes and source terms in all directions. We also choose a grid in which the resolution becomes more coarse with radius, as in our binary simulations. Specifically, we set $\delta r \propto r + 1$, we use 128 radial zones, and we keep $\delta\phi \approx \delta r$. Our choice of viscosity no longer allows a simple analytic solution for the time evolution of the fluid velocity, so we instead compare the velocity with the result of a high-resolution 1D code which solves the simplified fluid equation

$$\partial_t v_y(x, t) = \partial_x (v \partial_x v_y). \quad (25)$$

We find excellent agreement between the results of our *DISCO* run and that of the 1D code, as shown in Figure 2. In particular our implementation of viscous forces in *DISCO* is able to accurately capture the asymmetric spreading caused by a spatially varying viscosity.

3.2. Gas Dynamics Near the Binary’s Orbit

We restrict our attention to binaries with separations $a/M \gg 100$, so that we are in the pre-decoupling epoch in which the GW inspiral timescale is long compared to the viscous timescale, and orbital shrinkage can be ignored. We also note that the orbital decay due to interaction with the disk will be much slower than the viscous timescale in this regime (Kocsis et al. 2012a). Thus, we expect the flow to reach a quasi-steady state in which the size of the inner cavity is determined by the balance between gravitational torques and viscous stresses (Artymowicz & Lubow 1994; Milosavljević & Phinney 2005). In order to realize this quasi-steady state over the region of interest in our simulations, we must evolve for at least one viscous timescale

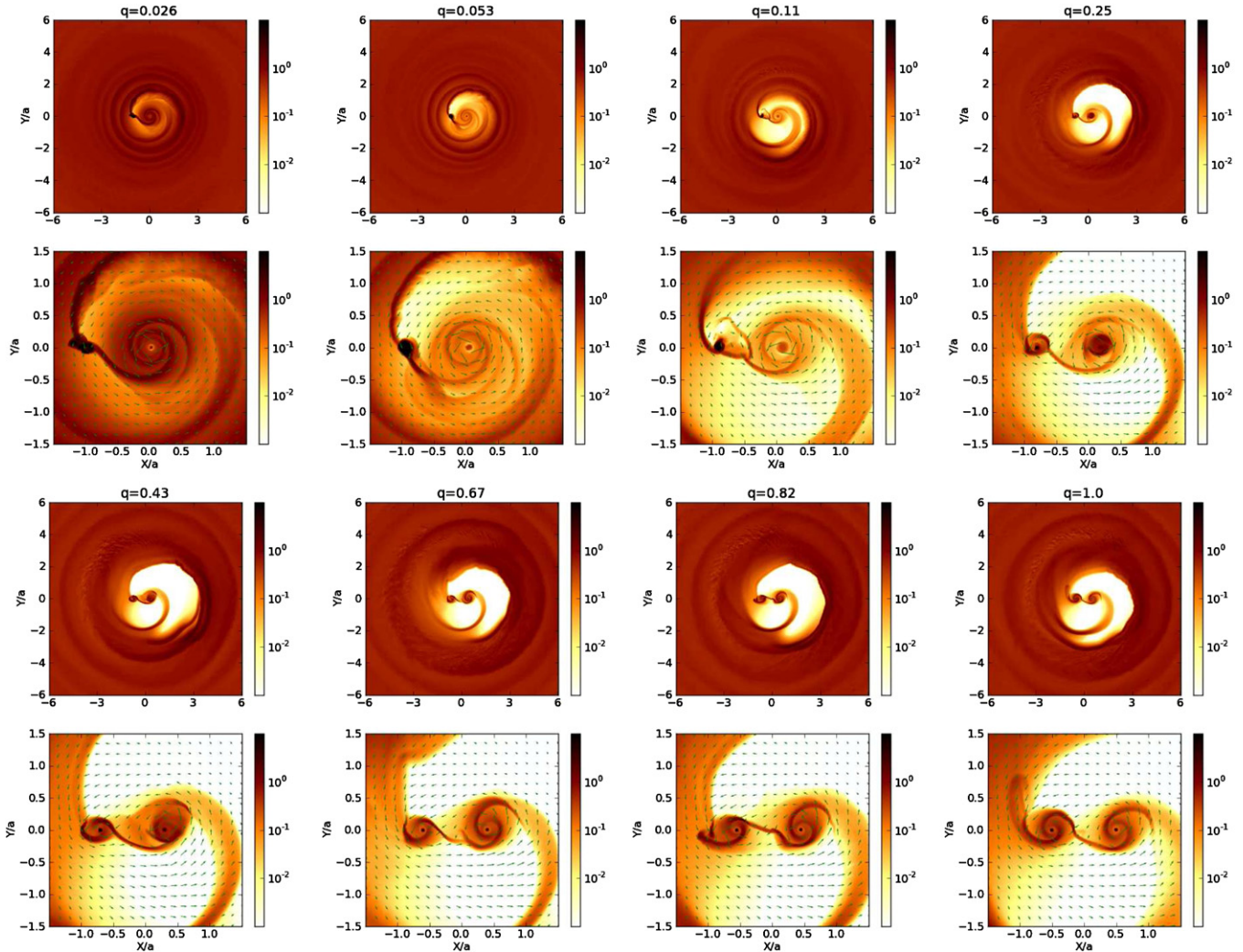


Figure 3. Snapshots of surface density Σ during quasi-steady state after $t \approx 460t_{\text{bin}} \approx 1.5t_{\text{vis}}$. Surface density is normalized by the maximum value at $t = 0$ and plotted on a logarithmic scale. For each snapshot, we plot both the inner $\pm 6a$ (top panel in each pair), and the inner $\pm 1.5a$ (bottom panel in each pair). Mass ratios are, from left to right and top to bottom, $q = 0.026, 0.053, 0.11, 0.25, 0.43, 0.67, 0.82$, and 1.0 . Orbital motion is in the counterclockwise direction. Green arrows represent fluid velocity.

(A color version of this figure is available in the online journal.)

at the radius of the cavity wall at $r/a \sim 2$

$$t_{\text{vis}}(r) \sim \frac{2}{3} \left[\alpha \left(\frac{h}{r} \right)^2 \Omega(r) \right]^{-1} \sim 300 \left(\frac{r}{2a} \right)^{3/2} t_{\text{bin}}. \quad (26)$$

In each of our simulations, we evolve for $\sim 1.5t_{\text{vis}}(2a)$. We find that this is sufficient in order to reach a quasi-steady state in the inner region of the disk, as reflected in relatively steady density profiles that we achieve after $t \gtrsim t_{\text{vis}}$. The mass ratios and time averaged accretion rates for each simulation are summarized in Table 1. Time averaged accretion rates are normalized by the time averaged accretion rate onto a single BH, \dot{M}_0 . We note that although the normalized accretion rate tends toward unity for small q as expected, it remains greater than unity for all cases considered. We caution that while these accretion rates remain steady over hundreds of orbits, we expect them to slowly relax to unity over much longer timescales as the outer regions of the disk relax to their quasi-equilibrium state. Thus, Table 1 should not be interpreted as evidence for binaries causing an enhancement in accretion. Rather, it should be interpreted as evidence that binaries are unable to fully clear a cavity and significantly suppress accretion, contrary to previous

Table 1
Summary of Mass Ratios and Average Accretion Rates

Mass Ratio q	$\langle \dot{M} \rangle / \langle \dot{M}_0 \rangle$
0.026	1.06
0.053	1.56
0.11	1.76
0.25	1.68
0.43	1.62
0.67	1.60
0.82	1.58
1.0	1.55

arguments (Milosavljević & Phinney 2005). We note that such arguments may underestimate the role that non-axisymmetric accretion streams play in allowing gas to penetrate into the cavity. Furthermore, binary torques may be responsible for moving gas near the inner disk edge onto more eccentric orbits, causing them to be captured by one of the BHs, thus increasing the accretion rate relative to that of a single BH.

Snapshots from each simulation are shown in Figure 3. In each case, a low density cavity is maintained surrounding the

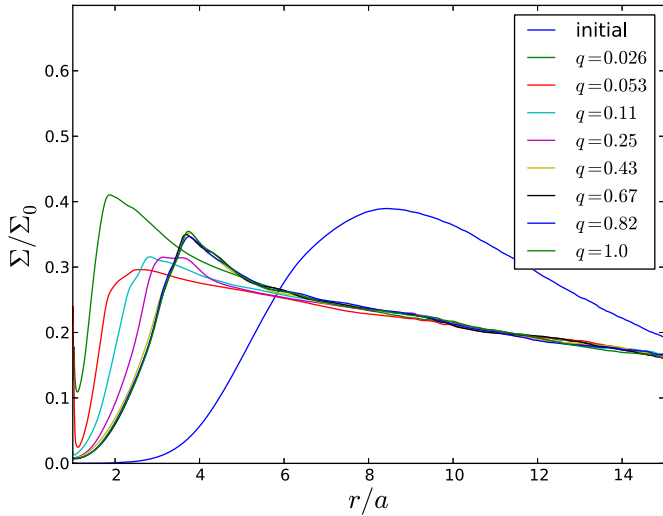


Figure 4. Time-averaged, angle-averaged surface density as a function of radius for various binary mass ratios. The blue curve is the initial surface density profile. Time average is taken over $446 < t/t_{\text{bin}} < 462$. We see that the size of the cavity increases with q , but approaches a near-constant profile for $q \gtrsim 0.43$. (A color version of this figure is available in the online journal.)

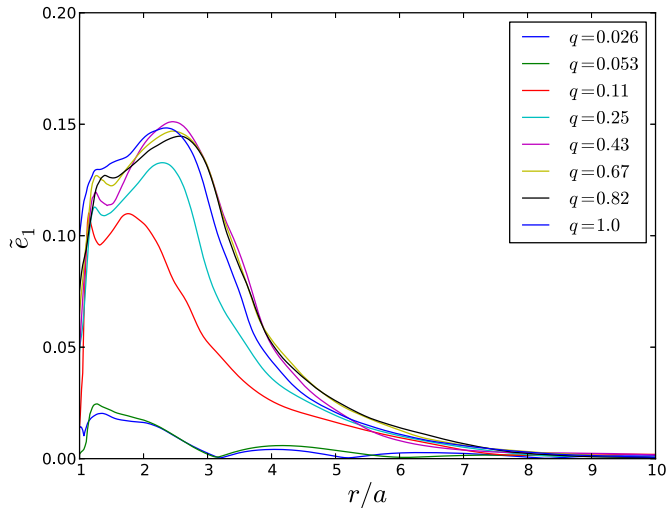


Figure 5. Time-averaged eccentricity \tilde{e}_1 as a function of radius for various binary mass ratios. Time average is taken over $446 < t/t_{\text{bin}} < 462$. Eccentricity is seen to increase with q .

(A color version of this figure is available in the online journal.)

binary, with the size of the cavity depending on the mass ratio q . We find that for $q \lesssim 0.25$, the cavity increases in size and eccentricity with mass ratio q . For $q \gtrsim 0.43$, both the size of the cavity and its eccentricity remain roughly constant. These trends are more obvious in Figure 4, where we plot time-averaged, angle-averaged 1D density profiles, and Figure 5 where we plot the time-averaged eccentricity profiles. We find that these profiles are very stable over the longest timescale of interest ($\gtrsim 100$ orbits) which corresponds to the time window over which we compute periodograms of the accretion rate. Here, we have used the definition of disk eccentricity provided by MM08, where we take the time-average of the density-weighted $m=1$ component of the radial velocity, normalized by the density-weighted azimuthal velocity,

$$\tilde{e}_m \sim \frac{|\langle \Sigma v_r e^{im\phi} \rangle|}{\langle \Sigma v_\phi \rangle}. \quad (27)$$

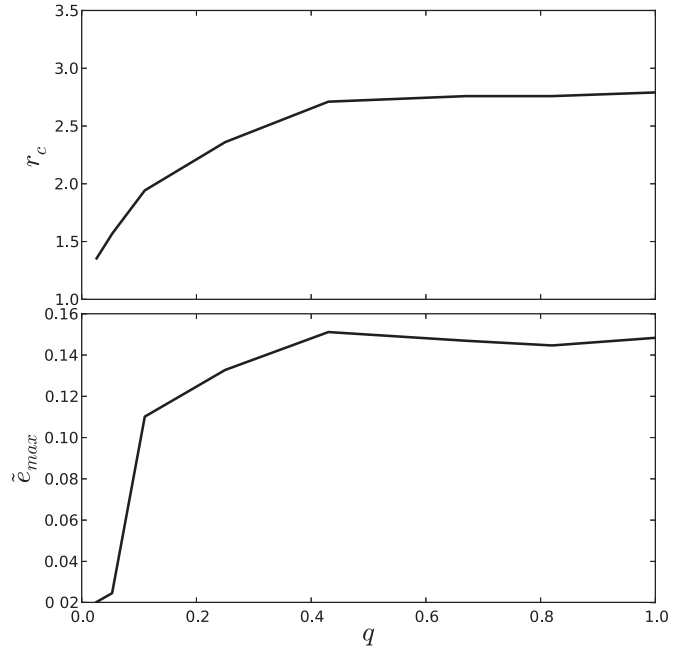


Figure 6. Maximum eccentricity \tilde{e}_{max} (bottom) and position of the outer edge of the cavity r_c (top), as a function of mass ratio q .

where,

$$\langle \cdot \rangle \equiv \frac{1}{2\pi} \int_0^{2\pi} d\phi. \quad (28)$$

We also plot the position of the outer edge of the cavity r_c (defined as the radius at which the $\Sigma = 1/2\Sigma_{\text{max}}$), and the maximum eccentricity \tilde{e}_{max} as a function of mass ratio q in Figure 6.

The trend toward an eccentric inner cavity for large mass ratio binaries has now been observed in a number of calculations (MacFadyen & Milosavljević 2008; D’Orazio et al. 2013; Shi et al. 2012; Noble et al. 2012; Farris et al. 2012). A plausible explanation for the growth of this eccentricity has been proposed by both Shi et al. (2012) and D’Orazio et al. (2013) and is summarized as follows. Torques from the binary create two streams which enter the cavity. A fraction of the gas in each stream does not accrete onto a BH, but rather is flung outward, impacting the cavity wall on the opposite side from which it entered. If one stream is perturbed and becomes larger, it will push the cavity on the opposite side outward, thus weakening the opposite stream. In this way, the imbalance grows and the inner cavity becomes eccentric. As we have focused on the limit in which $M_{\text{disk}} \ll M$ in this study, this disk eccentricity has no effect on the BH orbit. However, in future work we intend to relax this assumption, as this effect may indeed provide a mechanism for the growth of significant binary eccentricity, which may have important implications for GW observations.

We also note that the cavity is not truly evacuated, as substantial gas enters along streams and creates “mini disks” surrounding each BH. This can be seen in Figure 3, in which we plot snapshots of the surface density. We note that in many cases, the local surface density in these “mini disks” can exceed that of the circumbinary disk. It has been proposed that such mini disks can be observed as quasi-periodic active galactic nucleus sources (Artymowicz & Lubow 1996; Hayasaki et al. 2008, 2013). If the accretion timescale of a mini disk is short compared to the orbital timescale of the binary, each minidisk episode can mimic a stellar tidal disruption event (TDE), and, in case only a single

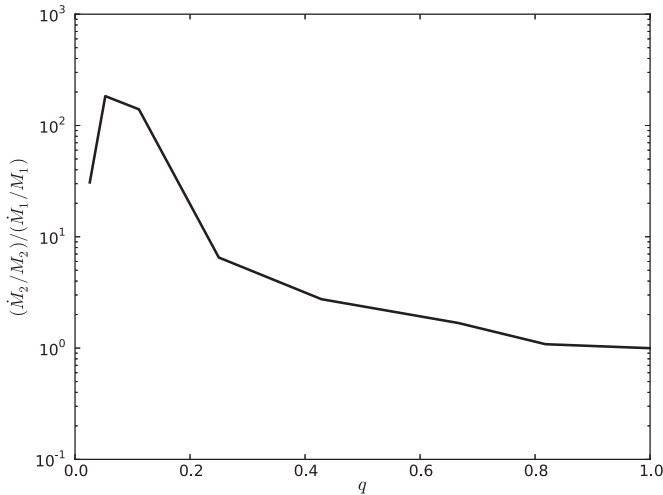


Figure 7. Plot of $(\dot{M}_2/M_2)/(\dot{M}_1/M_1)$ vs. BH mass ratio q . This quantity is > 1 when q is increasing, and < 1 when q is decreasing. For each case we find $(\dot{M}_2/M_2)/(\dot{M}_1/M_1) > 1$, indicating that mass ratios are always increasing with time. However, extrapolating the downward turn seen at small q , it is possible that there exists a threshold at small q , below which q decreases with time.

episode is detected, can even be confused with such a TDE (Tanaka 2013). In our simulations, we find that this is not the case, as the mini disks are relatively persistent. This is expected in light of our accretion prescription given by Equation (15). Scaled to an approximate mini disk size $r_{\text{md}} \approx 0.25a$, we find,

$$t_{\text{vis,md}} = 42 \left(\frac{\alpha}{0.1} \right)^{-1} \left(\frac{h/r}{0.1} \right)^{-2} \times \left(\frac{r_{\text{md}}}{0.25a} \right)^{3/2} \left(\frac{q}{0.1} \right)^{-1/2} t_{\text{bin}}. \quad (29)$$

We note, however, that the viscous timescale of each mini disk is sensitive to h/r , which we hold fixed at $h/r = 0.1$ in our model. In a more sophisticated treatment of the temperature, it is possible that the mini disks can become hotter and thicker, thus decreasing t_{vis} . If this heating is sufficient so that $h/r \sim 1$ in a mini disk, we see from Equation (15) that the viscous timescale can become $t_{\text{vis}} \sim 0.42t_{\text{bin}}$, and each mini disk will be effectively drained and replenished during each orbit. We also note that analytic work indicates that binary eccentricity tends to reduce the sizes of both circumpriary and circumssecondary mini disks (Artymowicz & Lubow 1994). This may also shorten the viscous timescale of each mini disk. We intend to address each of these points in future work.

3.3. Mass Ratio Evolution

An important question is whether the accretion is causing the mass ratio q to increase or decrease. The growth rate of q is given by,

$$\frac{dq}{dt} = \frac{d}{dt} \left(\frac{M_2}{M_1} \right) = \frac{M_2}{M_1} \left(\frac{\dot{M}_2}{M_2} - \frac{\dot{M}_1}{M_1} \right). \quad (30)$$

So we see that the condition for q to be increasing is that $\dot{M}_2/M_2 > \dot{M}_1/M_1$. In Figure 7, we plot the ratio $(\dot{M}_2/M_2)/(\dot{M}_1/M_1)$ as a function of q . We calculate \dot{M}_i for each BH by computing the total integrated rest mass removed during each timestep according to Equation (16). We find that for all simulations performed, this quantity is greater than unity, indicating that the mass ratio is growing, driving the binary closer

to equal mass. For the equal mass case ($q = 1.0$), we find that the ratio of accretion rates goes to unity, as expected. This result confirms the findings of a number of previous studies (Hayasaki et al. 2007, 2013; Cuadra et al. 2009; Roedig et al. 2011, 2012), all of which found greater accretion onto the secondary. Similar results have been found in simulations of gas accreting onto forming binary stars, provided the specific angular momentum of the accreting gas is sufficiently large (Bate & Bonnell 1997). We note, however, that the opposite has also been found in simulations of circumbinary accretion onto T Tauri binaries (de Val-Borro et al. 2011). The fact that $(\dot{M}_2/M_2)/(\dot{M}_1/M_1) > 1$ in our simulations is an important result, as it provides a mechanism for the distribution of mass ratios for massive BH binaries to be biased toward equal mass. Of course, the mass ratio can only grow significantly if the total accreted mass is at least as large as the initial mass difference between the primary and secondary.

It should be noted that while our smallest mass ratio, $q = 0.026$, corresponds to a binary with increasing q , the accretion rate onto the primary actually marginally exceeds that of the secondary. In this case, the accretion flow has taken on a qualitatively different form, in which the accretion flow resembles an annular gap with a large circumpriary disk (see Figure 3). Of course, this is the expected configuration for a binary with sufficiently small mass ratio, and has been well studied in the context of protoplanetary disks (Lin & Papaloizou 1993). We find that in this case the cavity is no longer completely cleared, and significant gas is able to flow past the secondary onto a dense circumpriary disk, and the accretion rate onto the primary has risen relative to the $q = 0.05$ case, and is slightly larger than that of the secondary (see first panel of Figure 9). This likely marks the beginning of a threshold in mass ratio q_{crit} below which the torque from the secondary is no longer able to effectively clear an entire hollow central cavity and the morphology becomes more similar to that of a disk with an annular gap. Extrapolating the results of Figure 7 to smaller mass ratios, $(\dot{M}_2/M_2)/(\dot{M}_1/M_1)$ may quickly drop below 1, although more simulations are required to verify this prediction. The value of q_{crit} is likely highly dependent on the disk thickness as it depends on gas flowing past the secondary without becoming gravitationally bound. Consequently, our value of $q_{\text{crit}} \sim 0.026$ should not be interpreted as a robust result applicable to all circumbinary disks. Nevertheless, this transition is important, because it may separate binaries into two categories: (1) large mass ratio binaries with $q > q_{\text{crit}}$ which are being further driven toward equal mass by enhanced accretion onto the secondary, and (2) small mass ratio binaries with $q < q_{\text{crit}}$ which may be further decreasing in mass ratio. This may lead to a bimodal binary mass-ratio distribution, with separate peaks at $q = 1$ and below q_{crit} .

In spite of the time variability of the “mini disks,” we can compare the time-averaged density profiles with analytic estimates of disk sizes based on perturbative calculations of disk truncation due to Lindblad resonances (Artymowicz & Lubow 1994). In Figure 8, we plot the time-averaged surface density profiles of the inner cavity region for the $q = 0.11$ and $q = 0.43$ cases (note that these are referred to as $\mu \equiv q/(q+1) = 0.1$ and $\mu \equiv q/(q+1) = 0.3$ in Artymowicz & Lubow 1994). We mark the analytic estimate of circumpriary and circumssecondary disk radii in cyan. In both cases, we find agreement with the analytic estimates, although we find that the circumpriary disk in the $q = 0.11$ case is strongly perturbed by the non-axisymmetric accretion streams.

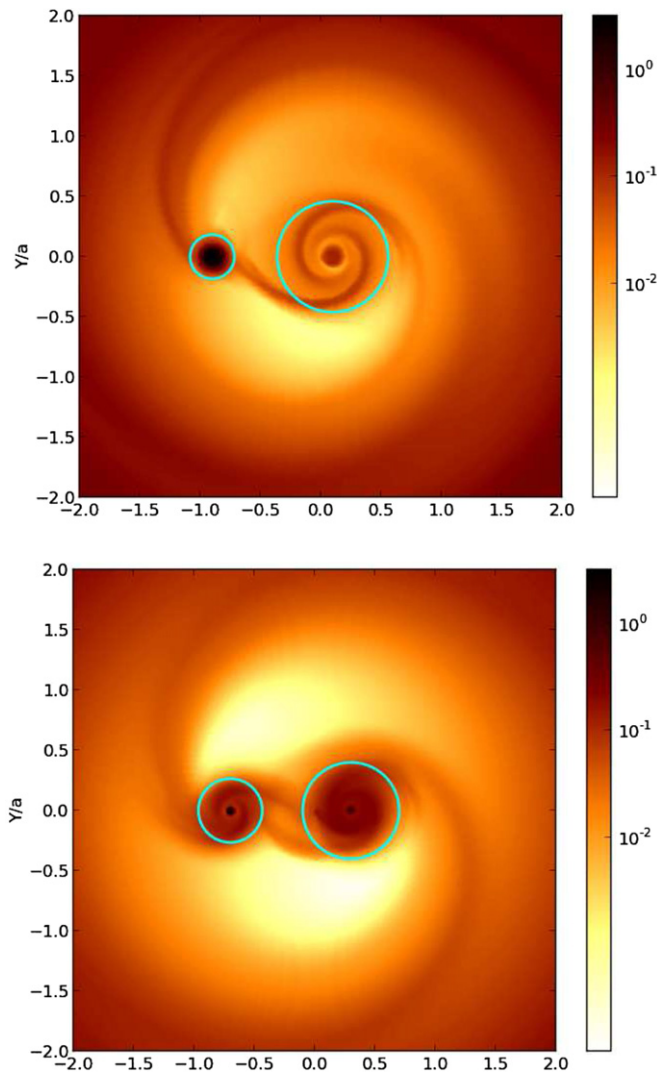


Figure 8. Time-averaged surface density Σ/Σ_0 . Cyan circles indicate the predictions of Artymowicz & Lubow (1994) for the size of the circumprimary and circumsecondary disks. Top figure is for a binary with $q = 0.11$ ($\mu \equiv q/(q+1) = 0.1$). Bottom figure is for a binary with $q = 0.43$ ($\mu \equiv q/(q+1) = 0.3$).

(A color version of this figure is available in the online journal.)

In Figure 9, we plot the accretion rate onto each BH versus time, as well as the Lomb–Scargle periodogram of the accretion rate for each mass ratio. We find many features in common with previous simulations in which the inner cavity at $r = a$ is excised from the grid and the total accretion rate is calculated through the inner boundary (MacFadyen & Milosavljević 2008; D’Orazio et al. 2013). For example, we find that significant periodicity in the accretion rate emerges for mass ratios $q \gtrsim 0.1$, with peaks in the periodogram at $\omega/\omega_{\text{bin}} = 1$ and $\omega/\omega_{\text{bin}} = 2$, consistent with the findings of D’Orazio et al. (2013) and Roedig et al. (2011). These peaks are straightforwardly interpreted as arising from the passage of each BH near the overdense lump which forms at the edge of the eccentric cavity and subsequent stripping of material and replenishment of accretion streams. For $q < 0.1$, these peaks are suppressed, as the binary torques are unable to excite eccentricity in the cavity and no noticeable overdensity is present. For $q = 1.0$, the peak at $\omega/\omega_{\text{bin}} = 2$ is present in the total accretion rate, but the peak at $\omega/\omega_{\text{bin}} = 1$ is present only in each individual BH accretion rate. The combined accretion rate

does not display this mode, as it is canceled by the symmetry of this case.

One notable feature of our simulations is the strength of the low frequency mode at $\omega_0/\omega_{\text{bin}} \approx 0.2$. For each case in which $q \gtrsim 0.43$, we find that this is the dominant component in the periodogram. We note that a similar feature is also seen in MM08, in Figure 12 of Roedig et al. (2012), and in the $\alpha = 0.1$, $q = 1$ case of D’Orazio et al. (2013). This low frequency component has been interpreted by MM08 as the orbital frequency of the overdense lump at the inner edge of the cavity. We also note that similar overdensities of gas near the inner wall of the cavity have been discussed in 3D MHD simulations by Noble et al. (2012) and Shi et al. (2012). Thus, any observation of periodicity in quasar emission is not likely to correspond directly to an associated binary period, but rather the orbital period of an overdense lump in the inner circumbinary accretion disk. In addition to the binary frequency and the lump frequency, we also find power in the associated harmonics. As in MM08, we find that for $q \gtrsim 0.43$, the total accretion rate can be decomposed into evenly spaced frequencies $\omega = \omega_0 K$, where $K = 1, 2, 3, \dots$

While the results of our simulations share some qualitative similarities with prior work, as described above, we find important differences. As our simulations do not excise the inner cavity, we are able to track the flow of the gas onto each mini disk, and track the accretion which takes place over a viscous timescale according to Equation (16). This is quite different from the accretion rate diagnostics employed in calculations which impose an inner boundary, in which \dot{M} is directly linked to the flux of rest mass through the inner surface at $r = a$. We find that the mini disks act as buffers, as gas accumulates in each mini disk and drains on a viscous timescale, rather than disappearing instantly upon entering the cavity. This smooths out the accretion rate and reduces the power in the periodogram at $\omega/\omega_{\text{bin}} = 2$. This is illustrated in Figure 10, in which we plot the accretion rate measured according to Equation (16), and the flux of rest mass through a surface at $r = a$, for comparison. We find that although the two methods agree on the average accretion rate $\langle \dot{M} \rangle / \dot{M}_0 = 1.6$, the latter dramatically overestimates the variability. This highlights the importance of the dynamics inside the cavity in determining time-dependent binary accretion signatures. We speculate that our inclusion of the inner cavity may also explain why our measured accretion rate of $\dot{M}/\dot{M}_0 = 1.55$ for the $q = 1$ case exceeds the corresponding measurement of 1.015 reported in Table 2 of D’Orazio et al. (2013). By including the inner cavity in our simulations, we allow fluid elements on eccentric orbits to approach the binary more closely and to be ejected toward the cavity wall with greater energy. This is expected to create a more eccentric cavity, which in turn causes the lump to approach the secondary more closely at periastron, thus allowing more gas to be stripped.

We have demonstrated that the periodicity in the measured accretion rate is strongly influenced by the presence of mini disks inside the cavity. The size and variability of each mini disk is, in turn, influenced by the temperature and viscosity inside the cavity, which determine the local accretion timescale. This link has been previously discussed by Sesana et al. (2012). While our choices of viscosity and temperature profiles are physically motivated, they are subject to some uncertainty, and it is worthwhile to examine how the accretion flow inside the cavity changes when t_{vis} is altered. To this end, we have restarted the $q = 0$ simulation from a checkpoint at $t/t_{\text{bin}} = 370$ and evolved for another ~ 100 orbits with the viscous timescale

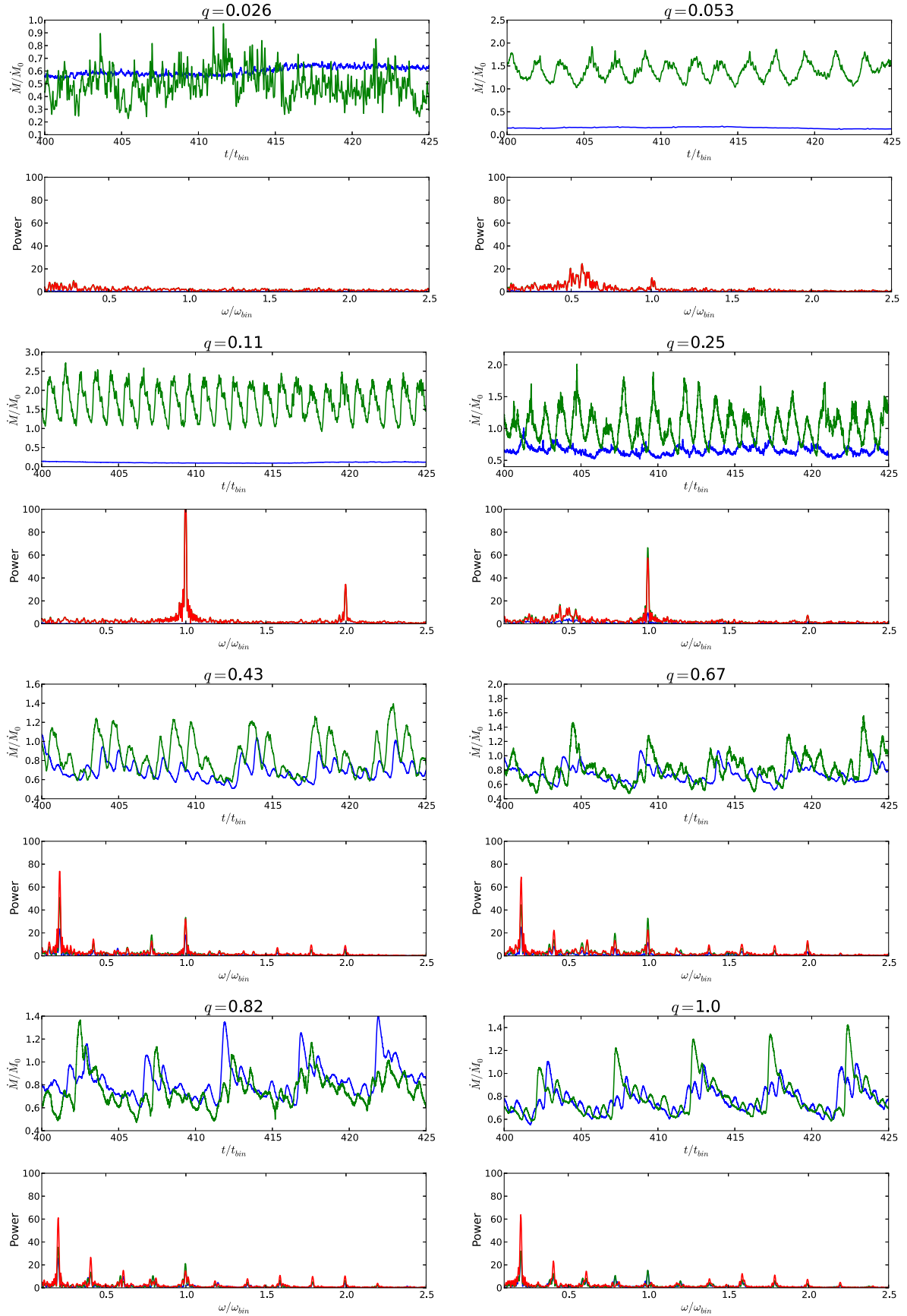


Figure 9. Time variable accretion rates onto each BH, measured using Equations (15) and (16) (top of each pair of panels) and the corresponding Lomb-Scargle periodogram (bottom of each pair) computed over ~ 100 orbits. From left to right and top to bottom, panels correspond to mass ratios $q = 0.026, 0.053, 0.11, 0.25, 0.43, 0.67, 0.82$, and 1.0 . In each panel, green lines correspond to the primary, blue lines correspond to the secondary, and red corresponds to the total accretion rate. (A color version of this figure is available in the online journal.)

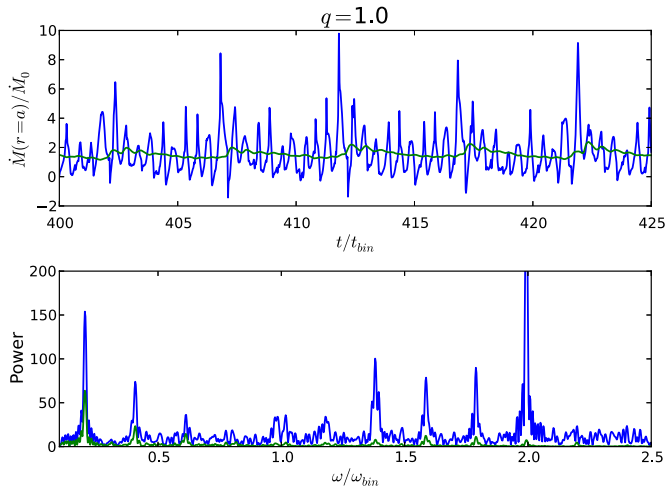


Figure 10. Total accretion rate \dot{M} through both black holes measured using two different methods. In the top panel in blue, we plot \dot{M} computed by measuring the flux of rest mass through a surface at $r = a$. In the top panel in green, we plot \dot{M} using Equations (15) and (16). In the bottom panel, we plot the corresponding periodograms. We see that measurements of \dot{M} that are performed at $r = a$ can overestimate the variability in the accretion rate.

(A color version of this figure is available in the online journal.)

t_{vis} from Equation (15) shortened by a factor of 100. From Equation (29), we see that this shortens the accretion timescale to less than the orbital timescale. Thus, any gas which is stripped during a passage with the lump should accrete within one orbit before having time to form a mini disk. Indeed, we see in Figure 11 a 2D snapshot of the surface density in which the mini disks are completely absent. This has the expected effect on the measured accretion rate, as the buffering effect of the mini disks is lost and the accretion variability is increased, as shown in Figure 12. In this case, the frequency at $\omega/\omega_{\text{bin}} = 2$ dominates, corresponding to the passage of the BHs past the lump which occurs twice per orbit. We emphasize that although the shortening of t_{vis} here is artificial, it is not implausible that such short timescales could be realized in nature. As $t_{\text{vis}} \sim (h/r)^{-2} \alpha^{-1}$, significant heating of the mini disk, or a mechanism for generating a large effective viscosity inside the cavity may significantly shorten t_{vis} . This underscores the need for future work to include more sophisticated treatments of the heating and cooling processes that determine the temperature inside the cavity, as well as precise treatments of viscosity that are motivated by studies of MHD turbulence.

For each mass ratio, we have computed the torque density profile following the definition provided in MM08,

$$\frac{dT}{dr} = \left\langle \frac{1}{2\pi} \int_0^{2\pi} \Sigma(r, \phi) \frac{d\Phi}{d\phi}(r, \phi) r d\phi \right\rangle, \quad (31)$$

and find that our results match those of MM08 very well for $q \gtrsim 0.43$ (See Figure 13). For lower mass ratios, we find that the peaks are shifted inward. This is consistent with the fact that smaller mass ratios lead to smaller cavities (see Figure 6). This is not surprising, as torques beyond $r/a \gtrsim 2$ should be much weaker for binaries with small q , and we expect the disk to be less distorted by a weaker perturber.

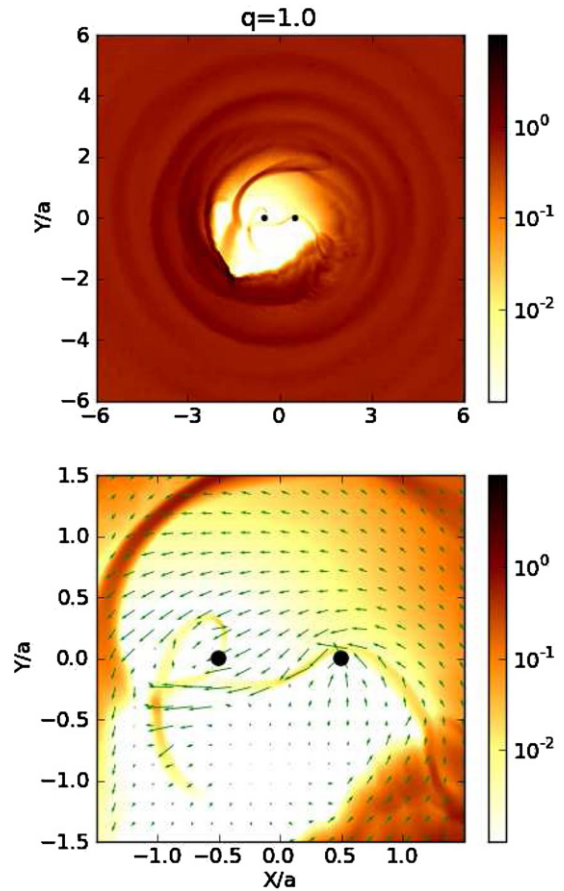


Figure 11. Snapshots of surface density Σ during quasi-steady state as in Figure 3, except that the simulation was run with t_{vis} shortened by a factor of 100, restarting the $q = 1$ run at $t = 370t_{\text{bin}}$ and running for another 100 orbits. By shortening t_{vis} so that it is less than t_{bin} , we find that “mini disks” are no longer able to form. We have added black circles to represent the locations of each BH.

(A color version of this figure is available in the online journal.)

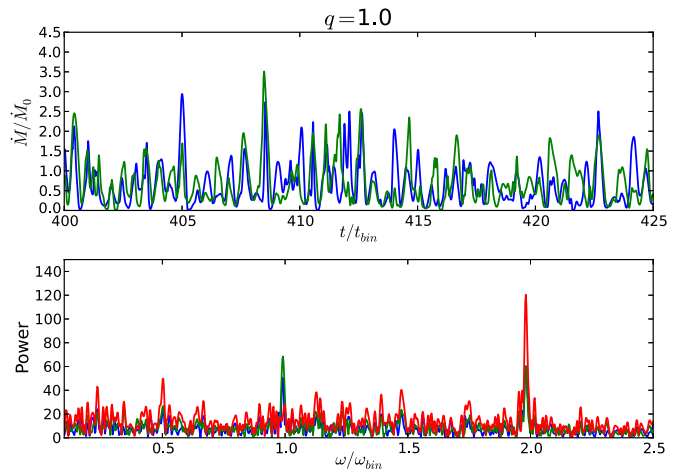


Figure 12. Time variable accretion rates and periodograms as in Figure 9, except that the simulation was run with t_{vis} shortened by a factor of 100, restarting the $q = 1$ run at $t = 370t_{\text{bin}}$ and running for another ~ 100 orbits. In the absence of any “mini disks” to act as buffers, absorbing infalling gas and delaying accretion, the accretion shows much greater variability, and is dominated by the $\omega/\omega_{\text{bin}} = 2$ mode.

(A color version of this figure is available in the online journal.)

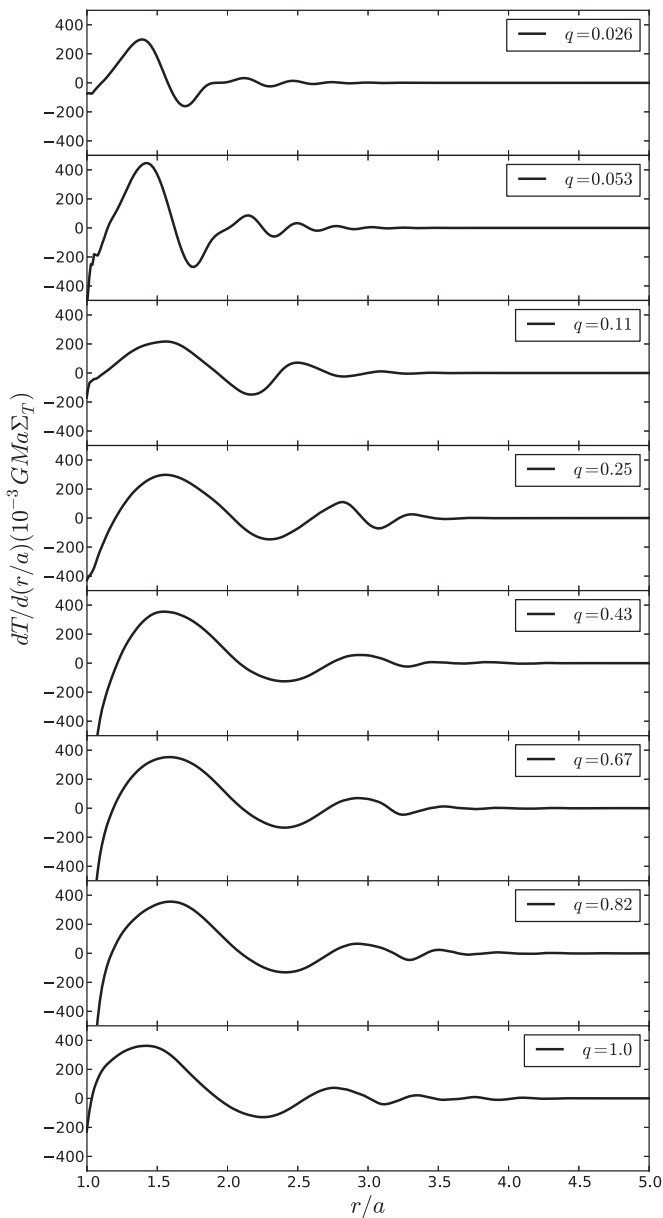


Figure 13. Time-averaged torque density dT/dr as a function of radius for various binary mass ratios. Each torque density is normalized by Σ_T , which is defined to be the time-averaged, angle-averaged surface density at the location of the first peak in dT/dr . Time average is taken over $446 < t_{\text{bin}}/M < 462$.

4. SUMMARY AND FUTURE WORK

4.1. Summary

We have performed the first hydrodynamic simulations of thin, circumbinary accretion disks using a moving-mesh, finite-volume code with the BHs present on the grid. Our disks are locally isothermal, corotating in the plane of the binary, and employ an α -law viscosity prescription. Our binaries are held at fixed separation in a circular orbit, and we simulate a range of mass ratios $0.026 \leq q \leq 1.0$. In each case, we ensure that we evolve for more than one viscous time at the inner edge of the circumbinary cavity, so that the inner accretion region has fully relaxed to a quasi-steady state.

The important results of this work are the following:

1. We confirm the finding of prior work (D’Orazio et al. 2013; Shi et al. 2012; Noble et al. 2012; Roedig et al. 2012) that

the accretion rate onto the BHs is not significantly reduced by the presence of a binary, when compared to the accretion rate onto a single BH of the same mass. This is the case in spite of the fact that much of the inner cavity is cleared of gas by the action of the binary torques, and is due to the effectiveness of the narrow accretion stream in delivering gas from the circumbinary disk inner edge to the individual BHs.

2. For each mass ratio considered, we find that “mini disks” surrounding each BH are formed. In each case, the mini disks are persistent, as their accretion timescale greatly exceeds the binary orbital timescale. However further work is required to determine whether or not this remains true when mini disks are allowed to become hotter. For the $q = 0.11$, and $q = 0.43$ cases, we confirm that the size of these mini disks is in rough agreement with the predictions of Artymowicz & Lubow (1994).
3. We find that significant periodicity in the accretion rates emerges only for $q \gtrsim 0.1$. At these mass ratios, the binary torques are strong enough to excite eccentricity in the inner cavity and create an overdense lump, whose interaction with the passing BHs leads to periodicity in the accretion rate. We find a strong peak in the periodograms for these cases corresponding to the orbital frequency of the lump, with many associated harmonics for the $q \gtrsim 0.43$ cases. This periodicity may constitute a unique observational signature of SMBH binaries.
4. We find that for each case considered here, the accretion rate onto the secondary is sufficiently large relative to that of the primary so that the mass ratio q is increasing. Similar results have been found previously in SPH calculations (Hayasaki et al. 2007; Cuadra et al. 2009; Roedig et al. 2011, 2012). As SMBHs are expected to gain a significant fraction of their mass through gas accretion (Soltan 1982; Yu & Tremaine 2002; Elvis et al. 2002), this suggests a mechanism which may bias the distribution of binaries near merger toward higher mass ratios.

4.2. Future Work

In future work, we intend to relax several assumptions, while expanding the parameter space of our simulations. In this paper we have assumed a locally isothermal equation of state with the temperature set such that $h/r \approx 0.1$ for both the circumbinary disk as well as each “mini disk.” This assumption should ideally be relaxed by incorporating a more sophisticated treatment of the temperature, so that the mini disks are allowed to heat or cool independently. This may have important consequences for the periodicity of the accretion, as the accretion timescale is sensitive to the temperature. If the accretion timescale becomes smaller than the binary orbital timescale, we may find that the accretion occurs in periodic outbursts, as discussed in Tanaka (2013). We also expect that realistic circumbinary disks may have a range of thicknesses, and we intend to investigate other choices for h/r .

In this work we have worked in the limit of $M_{\text{disk}} \ll M$, and thus kept the binary on a fixed circular orbit. In future work, this assumption should be relaxed in order to determine how binary eccentricity can be influenced by the eccentricity present in the inner disk. If significant eccentricity is imparted to the binary, it may have observational consequences for GW observations.

By working in the limit of $M_{\text{disk}} \ll M$, we have also neglected the shrinkage of the binary orbit due to interactions in the disk which can take place over long timescales (Kocsis et al.

2012a, 2012b). In future work, simulations should be done to characterize the coupled disk+binary evolution.

In each of our simulations, we have assumed that the orientation of the disk is aligned with that of the binary. Recent work done with SPH simulations of misaligned (or retrograde) disks indicate that dramatic differences may emerge when the binary is inclined with respect to the disk (Nixon et al. 2013; Roedig & Sesana 2013), but have yet to be compared with results of finite-volume simulations.

Finally, we have ignored BH spin in these calculations. In future work, including spin effects may modify the accretion flow onto individual BHs, and monitoring the change in the spin of each BH due to gas accretion may provide insight into models of binary BH spin distributions.

In summary, we have found that accretion flows surrounding BH binaries exhibit a host of complex features, including uneven BH growth rates which depend on mass ratio, potentially leading to biases in the binary BH mass-ratio distribution, as well as distinctive periodicity in BH accretion rates, which may provide a method of probing binary parameters through electromagnetic observations. Future simulations that incorporate the ingredients listed above will shed further light on these issues.

We would like to thank Daniel D’Orazio, Michael Kesden, Takamitsu Tanaka, and Aleksey Generozov for useful discussions. We acknowledge support from NASA grant NNX11AE05G (to Z.H. and A.M.) and by the NSF through grant AST-1009863 (to A.M.). Resources supporting this work were provided by the NASA High-End Computing (HEC) Program through the NASA Advanced Supercomputing (NAS) Division at Ames Research Center.

REFERENCES

- Amaro-Seoane, P., Aoudia, S., Babak, S., et al. 2013, *GW Notes*, 6, 4
- Armitage, P. J., & Natarajan, P. 2002, *ApJL*, 567, L9
- Artymowicz, P., & Lubow, S. H. 1994, *ApJ*, 421, 651
- Artymowicz, P., & Lubow, S. H. 1996, *ApJL*, 467, L77
- Barausse, E., & Rezzolla, L. 2008, *PhRvD*, 77, 104027
- Barnes, J. E., & Hernquist, L. 1992, *ARA&A*, 30, 705
- Bate, M. R., & Bonnell, I. A. 1997, *MNRAS*, 285, 33
- Begelman, M. C., Blandford, R. D., & Rees, M. J. 1980, *Natur*, 287, 307
- Bode, T., Bogdanović, T., Haas, R., et al. 2012, *ApJ*, 744, 45
- Chang, P., Strubbe, L. E., Menou, K., & Quataert, E. 2010, *MNRAS*, 407, 2007
- Cuadra, J., Armitage, P. J., Alexander, R. D., & Begelman, M. C. 2009, *MNRAS*, 393, 1423
- de Val-Borro, M., Gahm, G. F., Stempels, H. C., & Pepliński, A. 2011, *MNRAS*, 413, 2679
- D’Orazio, D. J., Haiman, Z., & MacFadyen, A. 2013, *MNRAS*, 436, 2997
- Duffell, P. C., & MacFadyen, A. I. 2011, *ApJS*, 197, 15
- Duffell, P. C., & MacFadyen, A. I. 2012, *ApJ*, 755, 7
- Duffell, P. C., & MacFadyen, A. I. 2013, *ApJ*, 769, 41
- Elvis, M., Risaliti, G., & Zamorani, G. 2002, *ApJL*, 565, L75
- Farris, B. D., Gold, R., Paschalidis, V., Etienne, Z. B., & Shapiro, S. L. 2012, *PhRvL*, 109, 221102
- Farris, B. D., Liu, Y. T., & Shapiro, S. L. 2011, *PhRvD*, 84, 024024
- Ferrarese, L., & Ford, H. 2005, *SSRv*, 116, 523
- Gammie, C. F. 1999, *ApJL*, 522, L57
- Giacomazzo, B., Baker, J. G., Miller, M. C., Reynolds, C. S., & van Meter, J. R. 2012, *ApJL*, 752, L15
- Goldreich, P., & Tremaine, S. 1980, *ApJ*, 241, 425
- Haehnelt, M. G., & Kauffmann, G. 2002, *MNRAS*, 336, L61
- Haiman, Z., Kocsis, B., Menou, K., Lippai, Z., & Frei, Z. 2009, *CQGra*, 26, 094032
- Hayasaki, K., Mineshige, S., & Ho, L. C. 2008, *ApJ*, 682, 1134
- Hayasaki, K., Mineshige, S., & Sudou, H. 2007, *PASJ*, 59, 427
- Hayasaki, K., Saito, H., & Mineshige, S. 2013, *PASJ*, 65, 86
- Hobbs, G., Archibald, A., Arzoumanian, Z., et al. 2010, *CQGra*, 27, 084013
- Ivanov, P. B., Papaloizou, J. C. B., & Polnarev, A. G. 1999, *MNRAS*, 307, 79
- Kocsis, B., Haiman, Z., & Loeb, A. 2012a, *MNRAS*, 427, 2680
- Kocsis, B., Haiman, Z., & Loeb, A. 2012b, *MNRAS*, 427, 2660
- Kocsis, B., & Sesana, A. 2011, *MNRAS*, 411, 1467
- Kormendy, J., & Richstone, D. 1995, *ARA&A*, 33, 581
- Krolik, J. H. 1999, *ApJL*, 515, L73
- Lin, D. N. C., & Papaloizou, J. C. B. 1993, in *Protostars and Planets III*, ed. E. H. Levy & J. I. Lunine (Tucson, AZ: University of Arizona Press), 749
- Liu, Y. T., & Shapiro, S. L. 2010, *PhRvD*, 82, 123011
- Lommen, A. N. 2012, *JPhCS*, 363, 012029
- MacFadyen, A. I., & Milosavljević, M. 2008, *ApJ*, 672, 83
- Masset, F. S. 2002, *A&A*, 387, 605
- Merritt, D., & Milosavljević, M. 2005, *LRR*, 8, 8
- Milosavljević, M., & Phinney, E. S. 2005, *ApJL*, 622, L93
- Müller, T. W. A., Kley, W., & Meru, F. 2012, *A&A*, 541, A123
- Nixon, C., King, A., & Price, D. 2013, *MNRAS*, 434, 1946
- Nixon, C. J., Cossins, P. J., King, A. R., & Pringle, J. E. 2011, *MNRAS*, 412, 1591
- Noble, S. C., Krolik, J. H., & Hawley, J. F. 2010, *ApJ*, 711, 959
- Noble, S. C., Mundim, B. C., Nakano, H., et al. 2012, *ApJ*, 755, 51
- Penna, R. F., Sądowski, A., Kulkarni, A. K., & Narayan, R. 2013, *MNRAS*, 428, 2255
- Roedig, C., Dotti, M., Sesana, A., Cuadra, J., & Colpi, M. 2011, *MNRAS*, 415, 3033
- Roedig, C., & Sesana, A. 2013, arXiv:1307.6283
- Roedig, C., Sesana, A., Dotti, M., et al. 2012, *A&A*, 545, A127
- Roos, N. 1981, *A&A*, 104, 218
- Sesana, A., Roedig, C., Reynolds, M. T., & Dotti, M. 2012, *MNRAS*, 420, 860
- Shakura, N. I., & Sunyaev, R. A. 1973, *A&A*, 24, 337
- Shapiro, S. L. 2010, *PhRvD*, 81, 024019
- Shapiro, S. L. 2013, *PhRvD*, 87, 103009
- Shi, J.-M., Krolik, J. H., Lubow, S. H., & Hawley, J. F. 2012, *ApJ*, 749, 118
- Soltan, A. 1982, *MNRAS*, 200, 115
- Springel, V., Di Matteo, T., & Hernquist, L. 2005, *ApJL*, 620, L79
- Tanaka, H., Takeuchi, T., & Ward, W. R. 2002, *ApJ*, 565, 1257
- Tanaka, T., Menou, K., & Haiman, Z. 2012, *MNRAS*, 420, 705
- Tanaka, T. L. 2013, *MNRAS*, 434, 2275
- Yu, Q., & Tremaine, S. 2002, *MNRAS*, 335, 965
- Yunes, N., Kocsis, B., Loeb, A., & Haiman, Z. 2011, *PhRvL*, 107, 171103